IMPROVEMENT OF THE TRACK-BASED ALIGNMENT PROCEDURE OF THE CMS MUON SYSTEM

An Undergraduate Research Scholars Thesis

by

NICK AMIN

Submitted to Honors and Undergraduate Research
Texas A&M University
in partial fulfillment of the requirements for the designation as

UNDERGRADUATE RESEARCH SCHOLAR

Approved by
Research Advisor: Dr. Alexei Safonov

May 2014

Major: Physics

TABLE OF CONTENTS

ABSTRACT

Improvement of the Track-based Alignment
Procedure of the CMS Muon System. (May 2014)

Nick Amin
Department of Physics and Astronomy
Texas A&M University

Research Advisor: Dr. Alexei Safonov
Department of Physics and Astronomy

The Compact Muon Solenoid (CMS) experiment at the Large Hadron Collider (LHC) is used to explore subatomic interactions through proton-proton collisions. The resulting outburst of particles from these high energy collisions is then tracked and analyzed through a sophisticated cylindrical layering of subdetectors. Proper alignment of the outermost subdetector on the endcaps of the cylinder, the Cathode Strip Chambers (CSC), is essential for an accurate reconstruction of momenta of various particles, especially for physics processes with muon signatures. The Reference-Target Algorithm developed and used by CMS for muon chamber alignment has been demonstrated to achieve a precision of better than 300-400 microns. However, the upcoming increase in beam energy of the LHC may allow production of new heavy particles that decay to TeV-scale muons, predicted, for example, in models that explain the weakness of gravity by new space dimensions. Optimization of the experiment's physics potential for higher energy calls for improved precision of muon alignment, which is currently limited by systematic effects. This study focuses on identifying the potential systematic effects, evaluating their impact, and proposing solutions or improvements to mitigate these effects.

DEDICATION

This thesis is dedicated to my parents, for their continued support and motivation.

ACKNOWLEDGMENTS

NOMENCLATURE

CERN	European Organization for Nuclear Research
CMS	Compact Muon Solenoid
CMSSW	CMS Software (Object-oriented C++)
CSC	Cathode Strip Chambers in the endcaps
DT	Drift Tube chambers in the barrel
IP	Interaction Point; the point of collision of the proton bunches
η	pseudorapidity; defined as $\eta = \ln(\tan(\theta/2))$ where θ is the polar angle with respect to the beamline, as viewed from the IP
LHC	Large Hadron Collider
ME	Muon Endcap. ME$\pm$ denotes the positive and negative endcaps with respect to the z coordinate
p_T	transverse momentum
tracker	central Silicon Tracker
strips	cathode strips in CSCs which run parallel to the radial vector from the beamline
wires	anode wires in CSCs which are perpendicular to the radial vector from the beamline

CHAPTER I

INTRODUCTION

Detector Overview

The Large Hadron Collider [1] was built to study fundamental particles and interactions. Through a worldwide collaboration, it was constructed at CERN in Geneva, Switzerland as a 27-kilometer diameter ring that accelerates protons in opposing directions around the ring to an energy of 4 TeV for each bunch that corresponds to speeds close to that of light. These bunches of protons then collide at predefined positions around the circular ring every 25 nanoseconds. Four major detector systems (Alice, ATLAS, CMS, and LHCb) were installed around these collision points in order to collect data from the high-rate and high-energy particle collisions. Due to the large amount of throughput data, a triggering mechanism employed on different levels helps to reduce the amount of stored data for later analysis.

The Compact Muon Solenoid (Figure I.1) is one of the two general-purpose detectors stationed on the LHC ring. The 13-meter long, 14-meter diameter CMS detector consists of layered detector systems, including central tracking elements, calorimeters, muon chambers, and a superconducting solenoid magnet [2]. The global coordinates for CMS consists of the directions x_{CMS}, y_{CMS}, and z_{CMS}, where x_{CMS} points south towards the center of the LHC ring, y_{CMS} points straight up, and z_{CMS} is oriented along the direction of the beam to the west. The sub-detectors of CMS comprise two endcaps and a single central barrel region, forming a cylinder. Detection of muons is handled by the muon system (Figure I.2), split into two major and distinct sub-systems: 468 cathode strip chambers in the endcaps of the detector and 250 drift tube chambers in the barrel region [3]. Additionally, there exist resistive plate chambers alongside these sub-systems which are used in the trigger mechanism, and will not be discussed here.
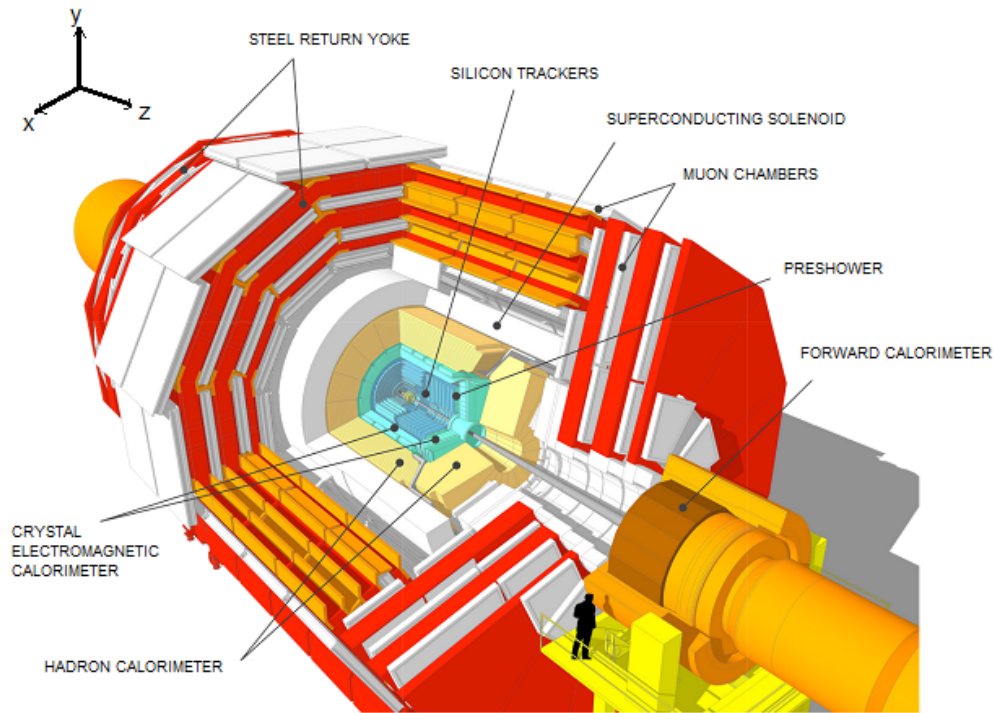
Fig. I.1. Pictured is a cutout of the CMS detector, displaying the layered layout, with the muon chambers in white on the outer portions of the cylinder. Protons travel parallel to the axis of the cylinder, and collide within the center of the silicon trackers [4].
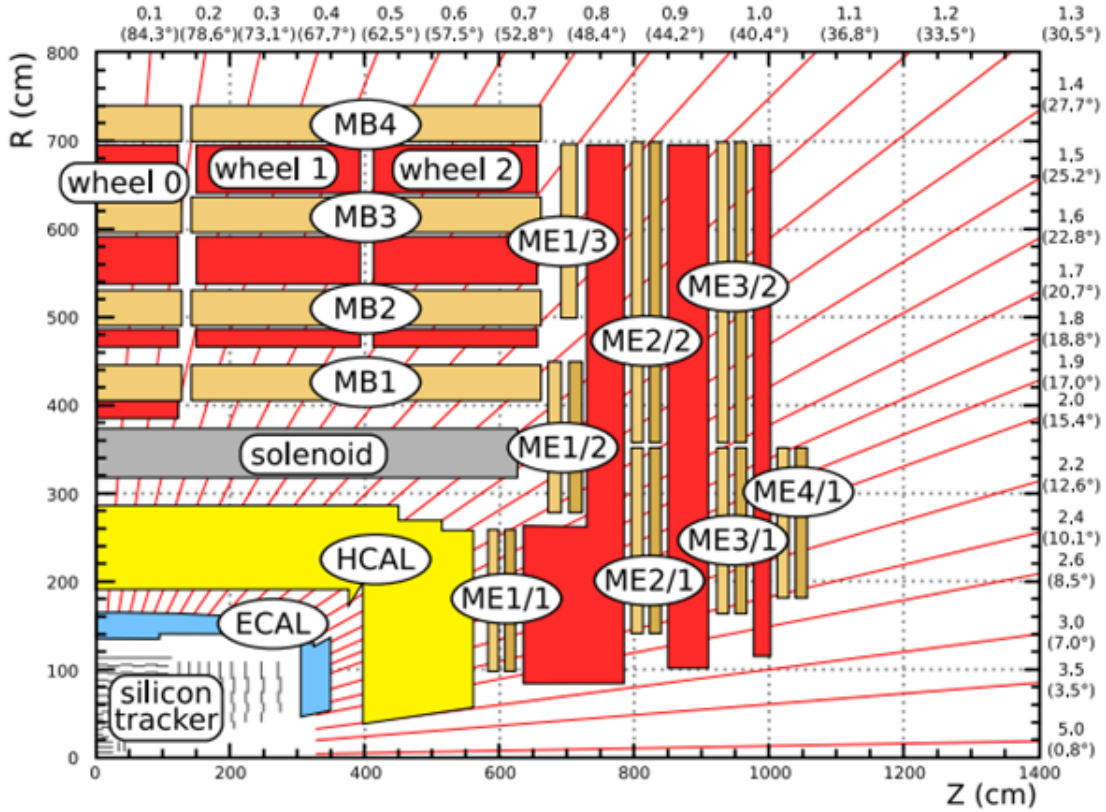
Fig. I.2. A transverse view of a quarter of the detector, where the R represents the distance from the beamline, and Z represents the distance along the beamline from the central collision point. The tan-colored muon endcap system on the right-hand side has 4 stations (ME1, ME2, ME3, ME4), each with several rings (e.g., ME2/1, ME2/2) [5]. ME4/2 (a fairly recent addition) is not pictured here.

Each trapezoidal CSC contains six layers of perpendicular rows of cathode strips and anode wires (Figure I.3). Thus, the detection of the charged muons [6] that pass through the muon system is done by collecting charges, from the muon's ionization of contained gas volumes, on the cathode and anode elements to provide two orthogonal coordinate measurements. Since there is the potential to have 6 of such 2-dimensional measurements, a 3-dimensional segment of the muon track can be constructed from the collected information.
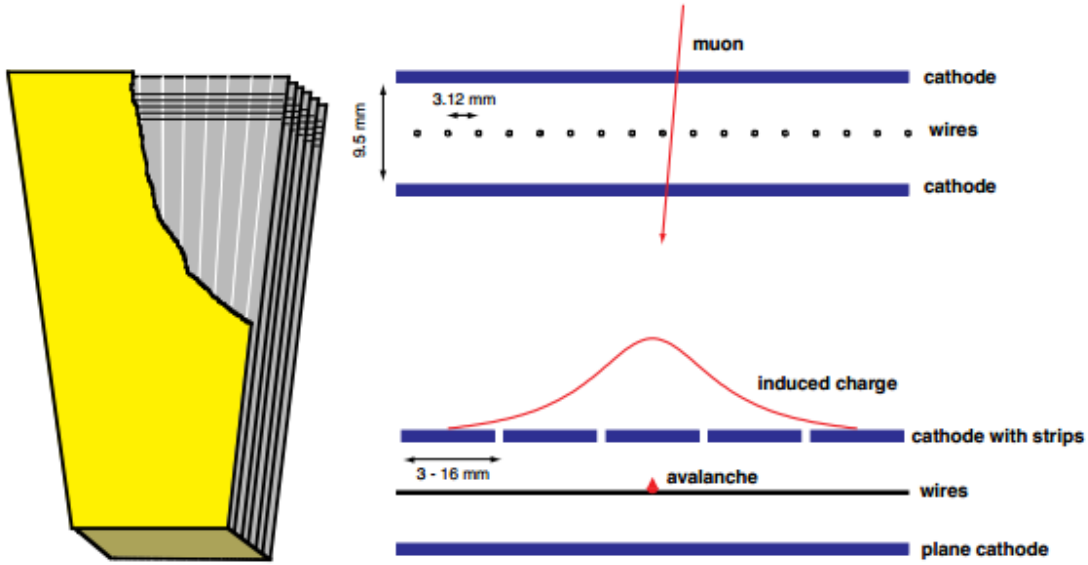
Fig. I.3. Left: Cutout of a single CSC, displaying the 6 layers of perpendicular strips and wires. Right: A muon track passes through these layers, ionizing the gas and causing charge to propagate towards the cathode strips and anode wires. The peak of the "avalanche" in both the strips and wires is measured to give the location of the passing muon [3].

Muon Alignment Overview

The muon system is crucial for reconstruction of physics processes that have muon signatures. As one could infer from the name, CMS was built to have excellent resolution for muon tracks with a broad range of transverse momenta, p_T, and pseudo-rapidity, η. Consequently, each constituent of the muon system must be aligned with respect to the central Silicon Tracker to within a few hundred micrometers in the direction of rotation around the axis of symmetry of the cylindrical detector ($R\phi$).

However, before the translational and rotational properties of any components of the muon system can be discussed in any meaningful way, appropriate coordinate systems must be established. The local coordinates for a CSC are depicted in Figure I.4. Local x runs along wires, local y runs along the central strip and local z is perpendicular to the chamber's sensitive layers.
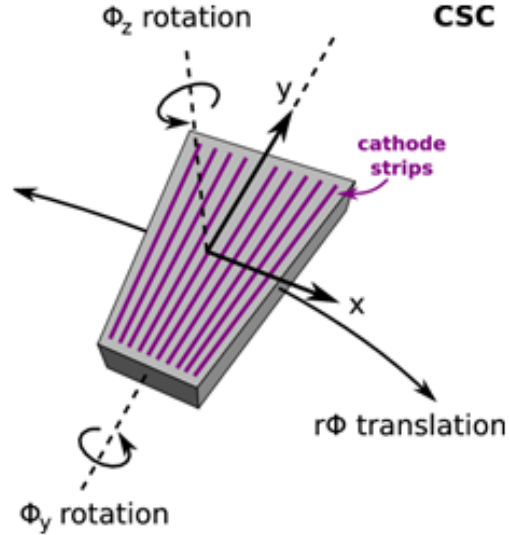
8

Fig. I.4. Local coordinates for a single CSC, with rotational notation. Local y points along the radial direction from the beamline, local x points along the $R\phi$ direction, and local z shares the same definition as the global z_{CMS}, but it is zero-centered at the chamber, instead of at the center of the CMS detector. ϕ_z represents rotation with local z as the rotational axis. Similarly ϕ_y represents rotation around local y and ϕ_x around local x [5].

There are two techniques that are currently employed to align the CMS muon system. Hardware alignment utilizes *in situ* optical and analog position measurements to determine relative shifting of the chambers to subsequently align the individual chambers [7]. Software-based alignment, on the other hand, uses a Track-Based (TB) alignment procedure utilizing real muon candidates in the collision data to perform a measurement of the muon chamber position and rotation using statistical methods [5]. The TB alignment procedure uses the Reference-Target algorithm, which utilizes muon tracks measured in the Silicon Tracker ("reference") and propagates these tracks to the muon system ("target"), taking into account the magnetic field. These propagated tracks can be compared with the actual hits observed in the muon system (Figure I.5) to measure deviations (called "residuals") which can be minimized over a large ensemble of muon candidates and fitted to obtain an optimal/aligned position for each muon chamber.
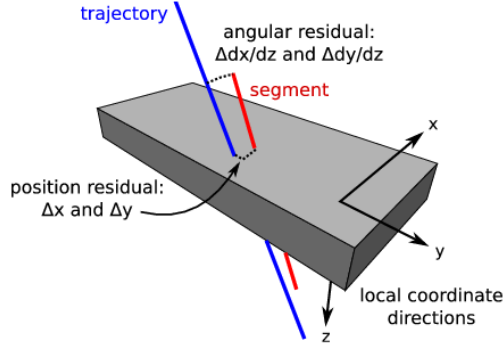
9

Fig. I.5. The main comparison done by the Reference-Target algorithm is illustrated in the sketch. Muon tracks propagated from the central tracker (in blue) are compared with the muon segment built from actual muon hits in the subdetector (in red). Differences in the x and y local spatial coordinates are labeled as residuals Δx and Δy, as well as the angular counterparts $\Delta dx/dz$ and $\Delta dy/dz$ [5].

This project focused on examining the low-level details of the alignment procedure in order to investigate possible causes of apparent systematic effects, which prevent further improvement of the accuracy of muon alignment measurements. Biases due to effects of the magnetic field on the post-alignment uncertainties are minimized by analyzing positive and negative muon tracks individually, and by dividing the analysis of muons into different ranges depending on the transverse momentum of the muons. Residuals on individual sensitive layers are studied to handle possible bias in chamber alignment from misalignment of internal structures. The principal data analyzed was collected during the 2012 runs of the LHC colliding beams operation. Developing software tools for such a pursuit became necessary for a chamber-based analysis of the alignment procedure.

CHAPTER II

METHODS

In several phases, the Track-Based alignment procedure turns collision data into alignment parameters in the form of a resultant muon system geometry that can be used as an input to subsequent processes, procedures, and analyses. In order to investigate systematic effects and noted pathologies, additional code was used in the software to collect previously unobtainable values. Such values were collected using recent data, and thoroughly analyzed with the aide of developed plotting mechanisms and programmatic tools.

Overview of the Track-Based Alignment Procedure

The alignment procedure first utilizes a "map" phase, where events in the input data are analyzed to find muons that pass through chambers of interest. Muon tracks that pass through a required number of chambers (given by a configurable threshold parameter) cause the procedure to calculate and store residual information, along with the muon properties. Residuals result from subtracting the location of the muon hit position and the location of a position from a propagation from the inner tracker into the muon system. Due to these relative calculations, the input data must be accompanied by an input geometry for the algorithm to calculate spatial differences on sensitive layers. Since event data for a large sample is typically stored separately in many files, the mapping phase can be run in parallel over these files by using accessible computing resources.

After the map phase, the "align" ("reduce") phase takes the stored residuals and event data and further filters the data by removing outlying residual information, relative to the mean of the distribution. Positive and negative muon counts are also equalized with respect to the p_T distribution to eliminate bias due to the magnetic field. The optimal positions of the chambers of interest are then computed through a multidimensional fit using MINUIT [8]

minimization software. For the endcap chambers, the average expected residuals are related to the misalignment parameters $(\delta x, \delta y, \delta z, \delta \phi_x, \delta \phi_y,$ and $\delta \phi_z)$ via the matrix equation,

$$
\begin{pmatrix} \Delta(R\phi) \\ \Delta y_0 \\ \Delta \frac{d(R\phi)}{dz} \\ \Delta \frac{dy}{dz_0} \end{pmatrix} = \begin{pmatrix} 1 & \left[-\frac{x}{R} + 3(\frac{x}{R})^3\right] & -\frac{dx}{dz} & -y\frac{dx}{dz} & x\frac{dx}{dz} & -y \\ 0 & 1 & -\frac{dy}{dz} & -y\frac{dy}{dz} & x\frac{dy}{dz} & x \\ 0 & -\frac{1}{2R}\frac{dx}{dz} & 0 & \left[\frac{x}{R} - \frac{dx}{dz}\frac{dy}{dz}\right] & 1 + \left(\frac{dx}{dz}\right)^2 & -\frac{dy}{dz} \\ 0 & 0 & 0 & -1 - \left(\frac{dy}{dz}\right)^2 & \frac{dx}{dz}\frac{dy}{dz} & \frac{dx}{dz} \end{pmatrix} \begin{pmatrix} \delta x \\ \delta y \\ \delta z \\ \delta \phi_x \\ \delta \phi_y \\ \delta \phi_z \end{pmatrix}.
$$

The output of this final phase mainly consists of geometry information for the post-alignment positions of chambers. Thus, the alignment procedure transforms an potentially misaligned input geometry into an aligned output geometry. By feeding the output geometry back into the alignment procedure as the next input geometry, subsequent iterations of the procedure should ideally converge onto the true geometry of the muon chambers.

Analysis of Misalignment of Sensitive Layers

The standard procedure treats chambers as essentially rigid objects, handling the tensions and biases in the fit, which indicate the presence of systematic effects. It therefore neglects possible misalignments of individual layers that form the muon chambers and cannot be used as is to investigate potential intra-chamber phenomena. This motivates designing a new software tool capable of looking at low-level details related to an individual chamber and effects related to its internal structure. The new procedure allows for rapid but detailed examination and study of intra-chamber phenomena, and the straightforward advent of custom information not present in the standard alignment procedure. In particular, residuals for each layer can be calculated. For this reason, a standalone analyzer, which reproduces the alignment procedure's residual calculation for a single chamber, was developed.

The workflow to analyze a chamber now consists of filtering single muon data from the 2012 runs of the LHC for a particular chamber. The filtered data is then run through a standalone analyzer written within standard CMSSW framework. The output of the analyzer is a ROOT [9] file containing muon parameters and residuals calculated on individual sensitive layers, which can be parsed using a Python script to produce various diagnostic plots.

Data Samples

Using data collected during the 8 TeV 2012 run (Table II.1), corresponding to a total integrated luminosity of approximately 20 fb^{-1}, a filter was run to select events which contained a muon passing through a chamber of interest. Events with at least one muon passing through the chambers of choice were retained, provided that the muon had at least 10 tracker hits, $p_T > 25$ GeV, and $|\eta| < 2.4$. The filtering procedure was completed for chambers 1, 17, 21, and 35 in the third ring of the first disk in each of the endcaps (i.e., ME$\pm$1/3/1, ME$\pm$1/3/17, ME$\pm$1/3/21, and ME$\pm$1/3/35).

Dataset	Date Filtered	Size	Events	Files
/SingleMu/Run2012A-MuAlCalIsolatedMu-22Jan2013-v1/ALCARECO	2013-02-05	219.7 GB	10610708	229
/SingleMu/Run2012B-MuAlCalIsolatedMu-22Jan2013-v1/ALCARECO	2013-02-07	1.3 TB	57312940	1206
/SingleMu/Run2012C-MuAlCalIsolatedMu-22Jan2013-v1/ALCARECO	2013-02-12	2.0 TB	85182667	1774
/SingleMu/Run2012D-MuAlCalIsolatedMu-22Jan2013-v1/ALCARECO	2013-03-04	2.2 TB	92216508	1947

Table II.1
Samples used for filtering.

Software Implementation

A standalone analyzer was first developed, which processes input data by looping through tracks for each event, propagates tracks into the endcap muon system and compares these values with the actual location of the muon hits in the endcap chambers. The differences

constitute the residuals for the local x and y coordinates. These 3 types of values (predicted hit position from propagated trajectory, actual hit, residual) for both coordinates on all layers where measurements exist, chamber identifier, p_T, p_z, and muon charge, were stored in the output ROOT file. Additionally, the analyzer could be configured to run over an entire ring of a given endcap and disk, as opposed to just a single chamber. In this study, ME±1/3 ring was of particular interest. The complete functionality of the analyzer was then moved into the canonical alignment procedure, utilizing the built-in track loops, event selection, and propagation methods. Thus, running the alignment procedure produces a ROOT file of layer information in parallel.

To eliminate existing misalignments, the alignment procedure was run with 3 iterations over 2012 data samples to produce an aligned geometry. This geometry was then used as the input for "map" jobs running over chambers of interest for this study. Using a pre-aligned geometry allows for inspection of relative effects within the chamber.

Muon Residuals

The output file from the "map" phase with layer information can be quickly run through a Python script to produce nine main types of plots, seven of which exist for each layer. Due to the direction muons are bent by the magnetic field, local x measurements mostly contribute to the measurement of transverse momenta. There is also less uncertainty on local x values because they are measured by cathode strips as opposed to the local y values measured by anode wires combined in coarse groups. Consequently, focusing on x residuals when plotting proves more fruitful. Note that $R\phi$ residuals can be calculated from x and y residuals via

$$\Delta R\phi = \Delta x \cdot cos(\phi) + \Delta y \cdot sin(\phi),$$

where $\Delta R\phi, \Delta x$, and Δy represent the residuals and ϕ is the angle, relative to a vertical line through the center of the chamber, of the strip and wiregroup where the hit occurred.

The main types of plots per layer are the following (illustrated in Figure II.1):

14

1. 1D x residual histogram

2. 1D $R\phi$ residual projected onto local y

3. 1D x residual projected onto "local" R

4. 1D x residual projected onto "local" $R\phi$

5. 1D x offset value for each layer

6. 1D rotational offsets for each layer

7. 2D actual (detected) hit position heat map

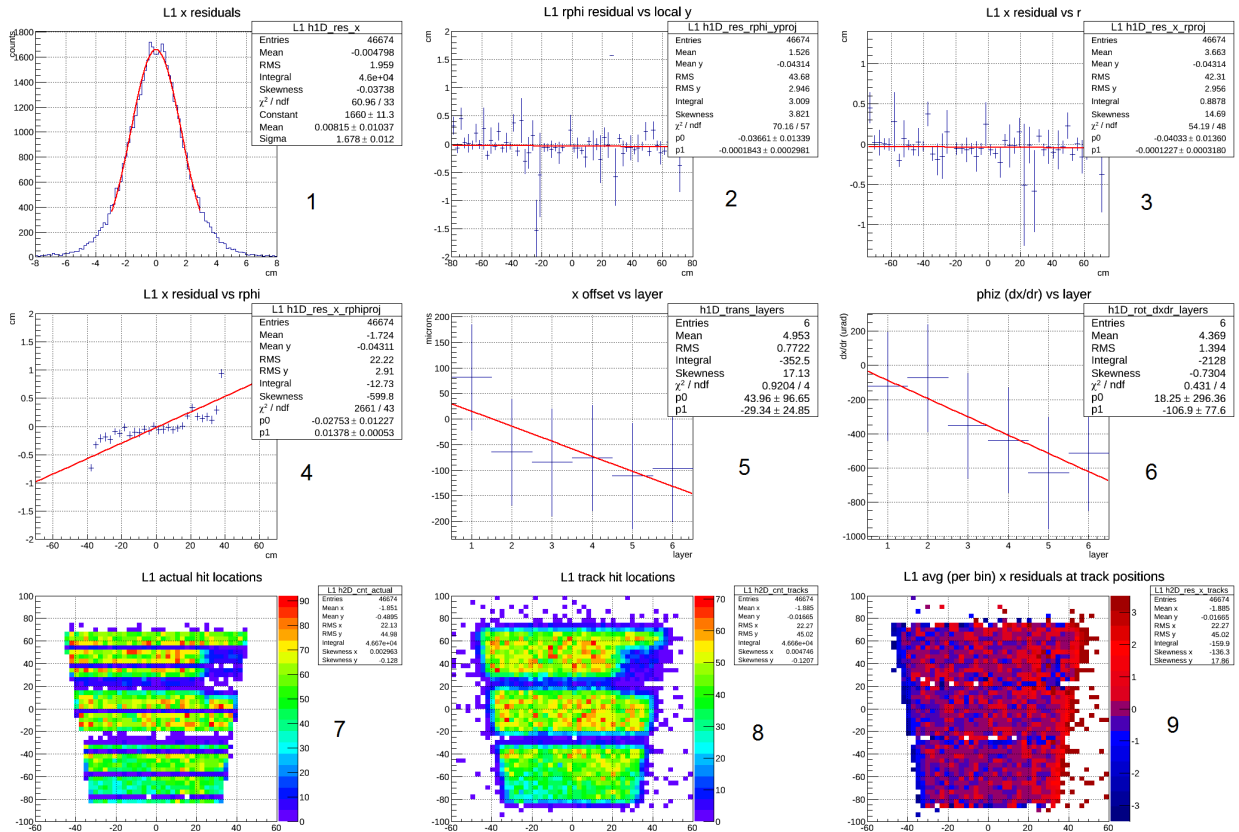8. 2D propagated track position heat map

9. 2D x residual heat map

Fig. II.1. The nine types of plots for layer 1 of the ME+1/3/17 chamber

Two-dimensional "occupancy" plots, are created by performing a discretization of a parameter at various locations on the chamber and using the third axis (color) as a measure of the average value of the parameter at that location. Projecting these heat maps onto perpendicular coordinates ("local" R and "local" $R\phi$) yields information about how the chamber's sensitive layers statistically tend to rotate or shear. Note that projecting residuals onto $R\phi$ actually consists of projecting them onto the angle multiplied by a constant, where the angle is calculated from the track positions and the scaling constant is a single, particular, radius of the chamber. For the ME+1/3 ring, the particular radius chosen was of the alignment pin, which resides at $R = 595.1500$ cm from the beamline.

By making the projected values of x residuals constant and at zero offset, one can find a rough value of the translational offset and rotational parameters of the chamber's position. In addition, a quick glance at the mean of the distribution of the x residuals reveals the x offset of the chamber.

Unlike the standard alignment procedure's output, the plots here are designed to show layer information. For example, one can observe that layers are rotated relative to each other. As standard alignment deals only with the chamber as a single rigid body, such an effect may not be appropriately dealt with, and could possibly result in undesirable uncertainties.

Consequently, applying a Gaussian fit to the 1D x residual histogram for each layer, we can produce a value for the translational offset of that particular layer. These values are then taken and summarized in an overview plot which shows the offsets for all 6 layers. From this, it is simple to visually inspect any shearing effects which might be present. Similarly, by performing a linear fit of the projection of $R\phi$ residuals (or local x residuals) onto R (x residuals vs local y), we can obtain the slope ($\frac{dx}{dR}$) that gives a rough measure of how much the layers desire to rotate about an axis through the chamber's center, perpendicular to the face of the chamber. Slopes of the linear fits are then summarized in an overview plot for visual inspection.

Boundary Effects

The plotting routine has a configurable option to make fiducial selection requirements that exclude boundary and low occupancy regions (Figure II.2). When tracks from the tracker are propagated into the muon system, they are allowed to lie outside of the physical bounds of the chamber (for example, shown in Figure II.2 as hits with local y values greater than approximately 85 cm). When comparing actual hits in the muon system, which will always lie within the chamber bounds, with the propagation track, there will be an unphysical offset (Figure II.3). Thus, boundary regions are susceptible to biases due to the propagation of tracker tracks.
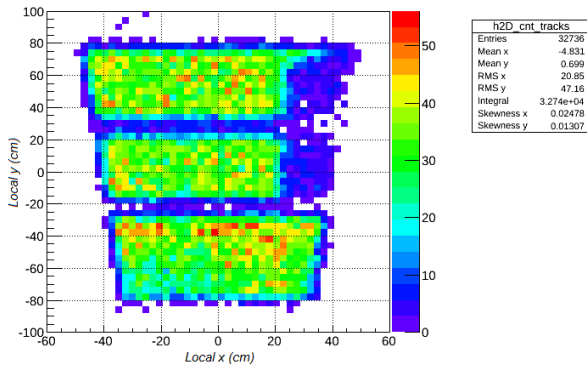

Fig. II.2. The propagated muon position occupancy plot for ME+1/3/17 shows low occupancy on all edges, including two horizontal strips associated with spacer bars within the chamber with little to no occupation. A particular low-occupancy region of study exists on the upper half of the right side.
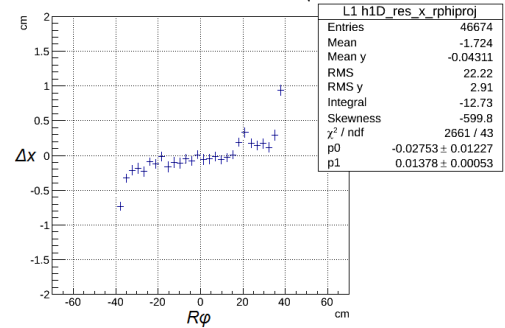

Fig. II.3. x residual vs $R\phi$ for ME+1/3/17 for layer 1, showcasing boundary effects on the left and ride edges of the chamber

Additionally, prior to plotting, the chamber can be artifically rotated, and the residuals can be recalculated. By attempting to minimize rotation effects and offsets, this effectively allows for a manual alignment of the chamber. Exploiting this, rotational effects can be explored in depth and compared to the standard alignment procedure.

Effects from Magnetic Field

Similar plots can be made for only positively-charged muons by filtering out negatively-charged muon events (and vice versa). As expected, distributions of x residuals have tail regions in opposite sides because of the opposite deflection of positive and negative charges in the magnetic field. From the data, one sees that there are approximately 15% more positive muons than negative muons, due to initial abundance of positive charges in proton-proton collisions. However, the standard alignment procedure eliminates the bias by analyzing an equal amount of positive and negative muon tracks.

Potential Operations and Instrumentation Pathologies

By examining an overview of the ME+1/3 ring, potentially problematic chambers can be identified and analyzed. Additionally, classifications of causes of alignment issues can be constructed. In total, three types of problems are evident from the ME+1/3 ring.

Low occupancy wedges

Demonstrated by every third chamber (in particular, chambers 17 and 35), these low occupancy wedges on one side of the chamber are due to effects related to interplay between triggering mechanisms in the muon barrel and endcaps (Figure II.4).

Low occupancy radial strip

Low occupancy regions in the radial direction are due to malfunctioning cathode strips, which run parallel to R. For example, chamber 11 has a set of malfunctioning strips (Figure II.4).

Lack of six-layer hits

The lower portion of chamber 21 has hits that only pass through an average of 5 layers in the chamber (Figure II.5). Additionally, each chamber has two thin, azimuthally-oriented regions with tracks measured on a total of 5 layers. This is due to spacers between wire groups creating insensitive regions that prevent all six layers from regis-

tering a hit. As the alignment procedure only retains tracks with six layers hit, these regions are filtered out.

Such occupancy issues can adversely affect the standard alignment procedure; therefore, studying the particular chambers in the ME±1/3 rings (1, 17, 21, and 35) discussed previously can shed light on alignment effects and possible ways to quell associated biases.
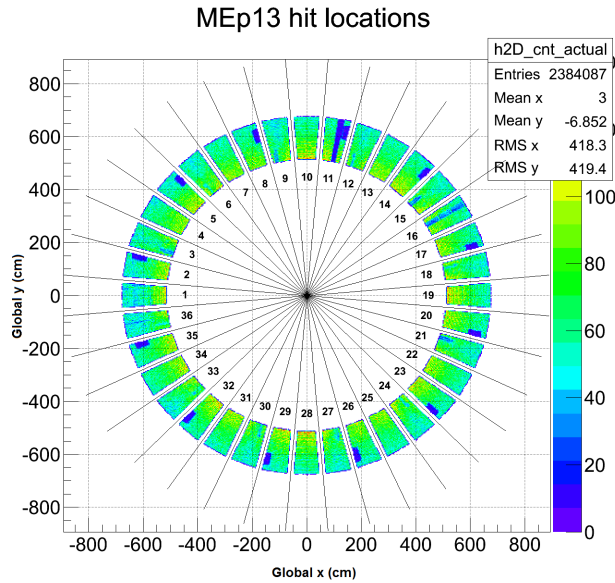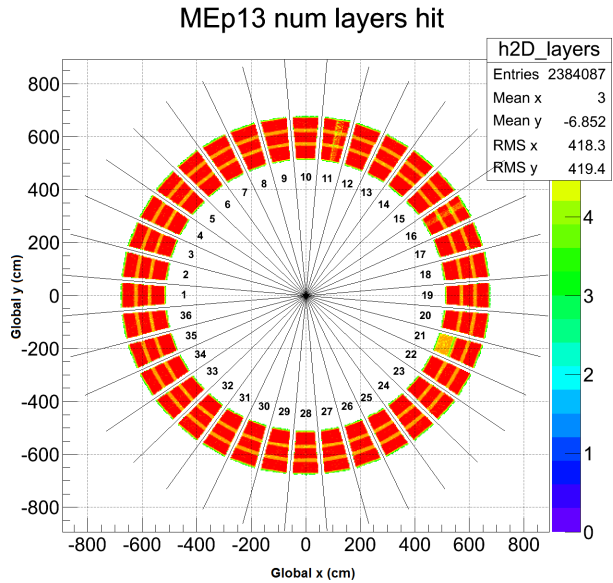

Fig. II.4. Hit occupancy plot for entire ME+1/3 ring.

Fig. II.5. Number of layers hit for entire ME+1/3 ring.

CHAPTER III

RESULTS

Through the course of systematic studies of the alignment procedure's handling of the endcap muon system, a number of possible causes of large uncertainties or biasing were uncovered. Most notably, these involve physical effects due to the internal geometry and occupancy of hits in the chambers.

Event Prefilter

Prior to "map" jobs in the alignment procedure, an optional (configurable) prefilter can be run over the input data sample. The prefilter removes events that do not have at least one interesting muon track of high quality. This is quantified as a track with number of tracker hits matching or exceeding a configurable threshold number, and number of muon segments in DT **OR** CSC systems exceeding or matching threshold value. In the endcap system, this has the possibility of causing unintended effects.

Effects in ME+1/3 Ring

Figure III.1 shows that every third chamber, starting with chamber 2, has an inverted "L" shape of one less muon segment in DTs than the rest of the chamber. Similarly, every third chamber, beginning with chamber 3, has one less DT segment in the center portion of the chamber and along the inner radius of the chamber. There also appears to be no DT segments in the central portion of the inner edge of these chambers. Geometrically, both of these effects are due to the design of the barrel system and interplay with the endcap system on the level of the trigger. Each station in the last wheel of the barrel muon system has 12 DT chambers, and each ME±1/3 ring has 36 chambers. This naturally gives rise to edge effects of period 30° (3 chambers).

Unlike with DTs, Figure III.2 shows a fairly expected pattern for number of muon segments in CSCs. Most muon tracks only intersect with 1 CSC station (outer portions of the ME+1/3 ring). However, the lower radius regions have at least a total of 2 CSC stations along the muon's track. Referring to the cross-sectional view of CMS in Figure I.2, if we treat a muon trajectory approximately as a straight line from the IP at $R = z = 0$, we observe that muons will only make contact with the ME+2/2 ring if they roughly pass through the bottom half of the chamber. Additionally, a small amount of muons with a very low R will pass through ME+3/2. Odd numbered chambers in ME+1/3 show that 3 CSC station hits are achieved in the few centimeters of the chamber closest to the IP, but even-numbered chambers do not display such a trend. As the ME+3/2 ring has overlapping chambers in ϕ, they must be physically staggered in z, so some chambers are closer to the ME+1/3 ring (odds) and others are further away (evens), explaining the odd-even discrepancy. This effectively explains all CSC station occupancy effects as projected upon the ME+1/3 ring.
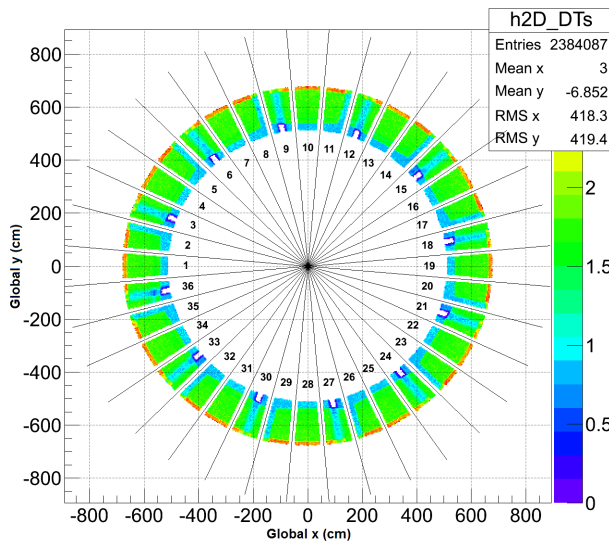

Fig. III.1. Number of DTs that a muon passed through, projected onto the actual hit position of the ME+1/3 ring.
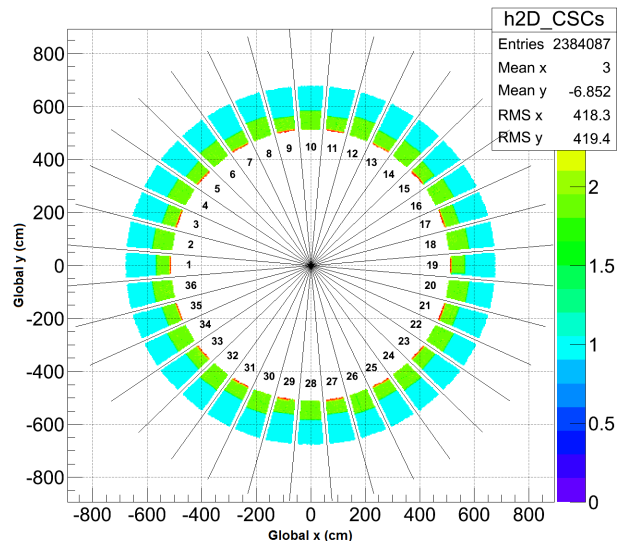
Fig. III.2. Number of CSCs that a muon passed through, projected onto the actual hit position of the ME+1/3 ring.

21

Effects in ME+1/3/17 Chamber

Combining these two effects helps explain the prefiltering effects in the alignment procedure. Ignoring the tracker hit requirement, an event must have a minimum number of muon segments in DT or CSC. As this is an "or" relation and not an "and", an excess of segments in one subsystem can compensate for a lack of segments in the other. For example, taking chamber 17 in the ME+1/3 ring, we can look at hit occupancy without any prefiltering (Figure III.3) using 2012 data and we observe that there is a low occupancy region at the top right (effect with period 30° in ME+1/3 ring). After the prefilter (Figure III.4), the low occupancy region has extended to the middle third of the chamber. Given the constraints from the prefilter, we would expect the low number of DT segments projected to this chamber (Figure III.1) to cause hits in the lower portion of the chamber to also be filtered out; however, the number of CSC hits in this portion exceeds the threshold, so all hits are retained in that region.
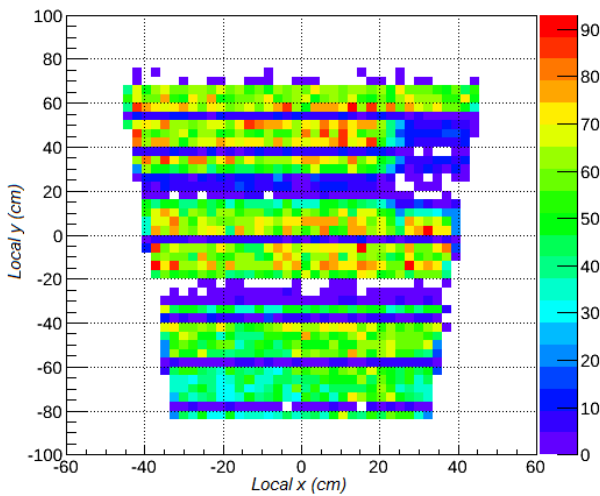

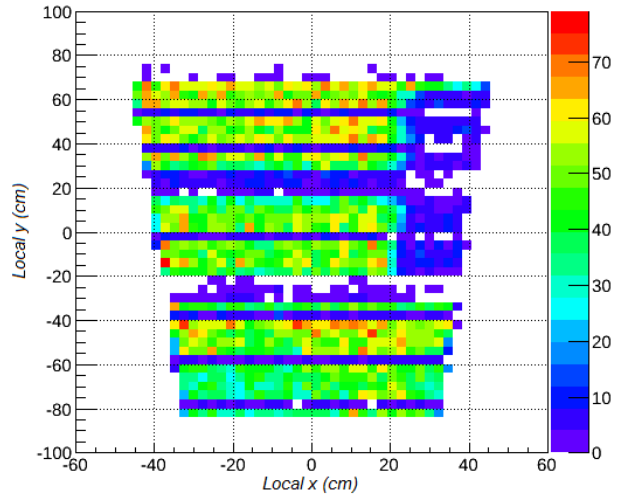Fig. III.3. Actual hit occupancy for ME+1/3/17 with no prefilter

Fig. III.4. Actual hit occupancy for ME+1/3/17 with prefilter

22

Result

Due to the structuring of the prefilter, the barrel system (DTs) can affect acceptable CSC muon hits. This introduces biases in the alignment procedure for the endcap chambers. Therefore, the requirement of having 2 or more muon segments in the prefilter was deemed undesirable to use in subsequent analyses (including those for this investigation).

Edge Effects

Muon tracks propagated from the inner tracker can end up outside of the physical chamber (Figure III.5), but physical hits are confined to the chamber by definition. Thus, near the edges of chambers, x residuals associated with edge tracks are large and one-side biased. This causes an overall surplus of one-sided residuals on the edges of the chamber. Essentially, a strong competitive pulling effect occurs at the two sides of the chamber.
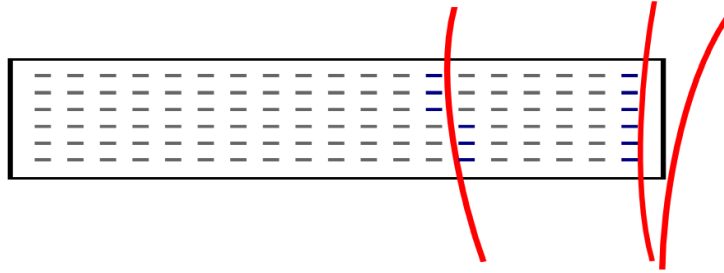

Fig. III.5. Cross-section of single CSC (perpendicular to strips). Red tracks are muon paths and blue shaded strips are those with the associated registered hit.

Looking at a 2D heatmap of average x residuals binned at propagated muon positions on layer 1 of ME+1/3/17, the pulling effect is apparent (Figure III.6). The magnitude of residuals on the two edges are as large as 3 centimeters, suggesting that these regions carry a significant weight in the alignment procedure. Going one step further to quantify these effects, average x residuals can be projected onto $R\phi$ slices to obtain a one-dimensional plot showing large diverging tails (Figure III.7).
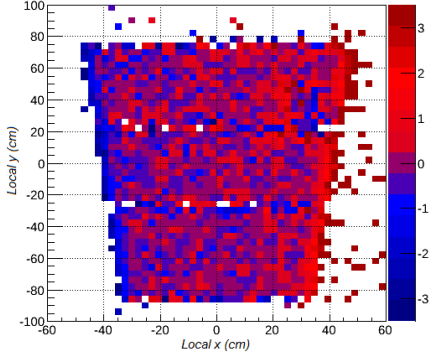
Fig. III.6. x residual heatmap for ME+1/3/17 layer 1. z-axis (color) represents average x residual in bin in centimeters.
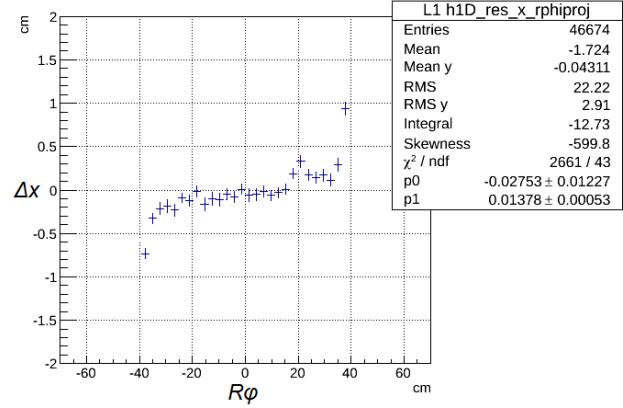

Fig. III.7. x residual vs $R\phi$ for ME+1/3/17 layer 1.

Chamber Fiducial Selection Requirement

To study the contribution of these edge effects on the translational and rotational alignment outcomes of the chamber, residual distributions were compared before and after a selection requirement on the edges was implemented. The selection requirement consists of discarding tracks with propagated positions with $R\phi > 28$ cm so that large residuals at edges are removed from chamber analysis. After the imposed selection, the analogous plot to Figure III.7 lacks diverging tails (Figure III.8). Evidently, there exists an artifact of the low occupancy box on the right edge of the chamber, as this creates an artificial edge, which will be handled separately.

The x offset for each layer is computed before and after the implementation of the requirement (Figs. III.9, III.10). Between the two, there is an overall shift of almost 200 microns. Similarly, before and after plots for ϕ_z rotation for each layer (Figs. III.11, III.12) show that an overall rotation of almost 1 milliradian is introduced. Relative rotations between layers is approximately preserved, as these edge effects are uniform through all six layers.
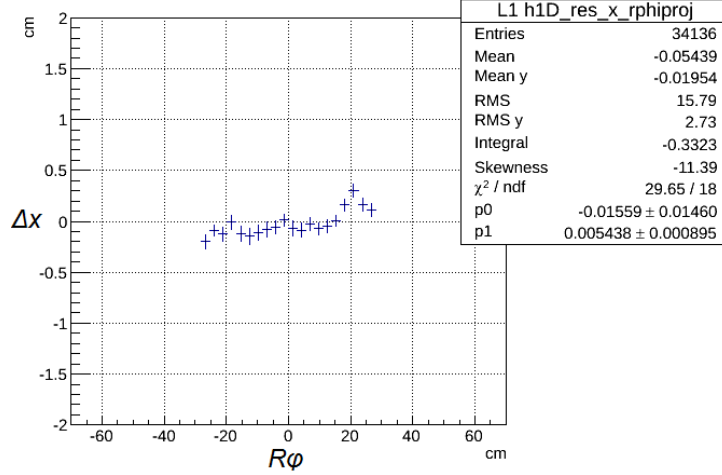
24

L1 h1D_res_x_rphiproj	
Entries	34136
Mean	-0.05439
Mean y	-0.01954
RMS	15.79
RMS y	2.73
Integral	-0.3323
Skewness	-11.39
χ^2 / ndf	29.65 / 18
p0	-0.01559 ± 0.01460
p1	0.005438 ± 0.000895

Fig. III.8. Layer 1 x residual vs $R\phi$ for ME+1/3/17 after $R\phi > 28$ cm requirement

Result

As the residuals on the edges have been shown to have a significant effect on the alignment of the chamber, any angular anisotropy of muon tracks along the chamber can preferentially pull the chamber to one side over the other. Thus, fiducial selection requirements along the sides of the chamber can eliminate such outcomes.

Effects from Low Occupancy Areas

Due to the periodic low occupancy regions in the ME+1/3 ring discussed earlier, chamber 17 has a low occupancy "box" on the upper right side of the chamber, as viewed from the IP. As previously shown (Figure III.7), there exist non-zero average x residuals at $R\phi \approx 20$ cm, consistent with the location of the low occupancy region. This agrees with described edge effects, as muon trajectories have no spatially symmetric hit partners in the chamber when they pass through the edge of the deficient region.
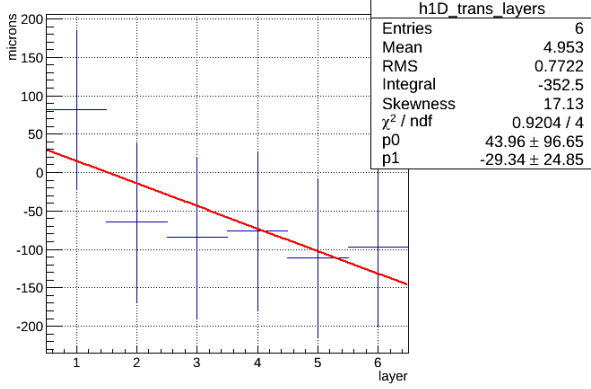
25

h1D_trans_layers	
Entries	6
Mean	4.953
RMS	0.7722
Integral	-352.5
Skewness	17.13
χ^2 / ndf	0.9204 / 4
p0	43.96 ± 96.65
p1	-29.34 ± 24.85

h1D_trans_layers	
Entries	6
Mean	2.987
RMS	1.678
Integral	868.3
Skewness	0.4206
χ^2 / ndf	0.2397 / 4
p0	234.2 ± 112.0
p1	-25.55 ± 28.83

Fig. III.9. Mean x residual (μm) vs layer number for ME+1/3/17 **without** edge selection requirement.
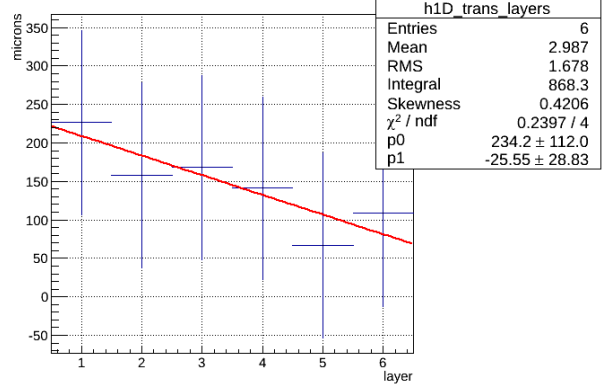
Fig. III.10. Mean x residual (μm) vs layer number for ME+1/3/17 **with** edge selection requirement.

h1D_rot_dxdr_layers	
Entries	6
Mean	4.369
RMS	1.394
Integral	-2128
Skewness	-0.7304
χ^2 / ndf	0.431 / 4
p0	18.25 ± 296.36
p1	-106.9 ± 77.6

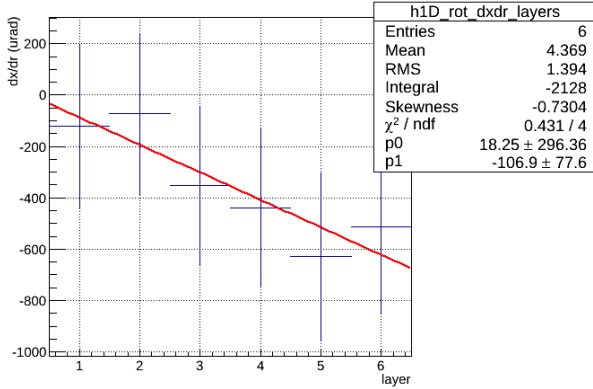| h1D_rot_dxdr_layers	
Entries	6
Mean	2.826
RMS	1.58
Integral	3019
Skewness	0.5543
χ^2 / ndf	0.1988 / 4
p0	912.2 ± 297.0
p1	-116.9 ± 76.6

Fig. III.11. Mean rotation ($\frac{d\Delta x}{dr}$) (μrad) vs layer number for ME+1/3/17 **without** edge selection requirement.

Fig. III.12. Mean rotation ($\frac{d\Delta x}{dr}$) (μrad) vs layer number for ME+1/3/17 **with** edge selection requirement.
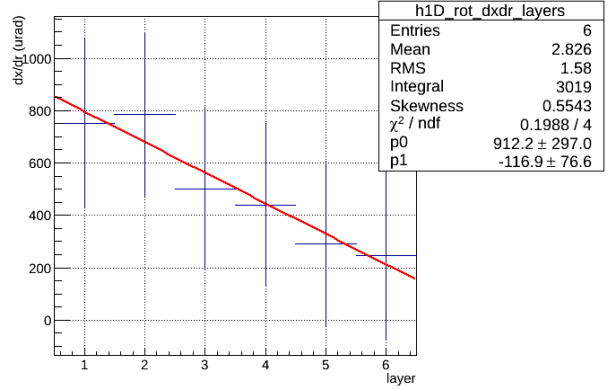
Low Occupancy "Box" Fiducial Selection Requirement

Implementing additional selection requirements on this region by discarding muons with trajectory $R\phi > 14$ cm and 20 cm $< y <$ 65 cm, comparisons can be made before and after the imposed selection requirement to assess the magnitude of the effect of this low occupancy region.
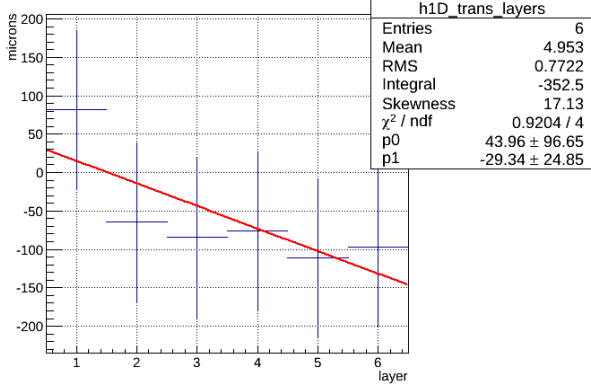
26

Fig. III.13. Mean x residual (μm) vs layer number for ME+1/3/17 **without** low occupancy "box" removed.
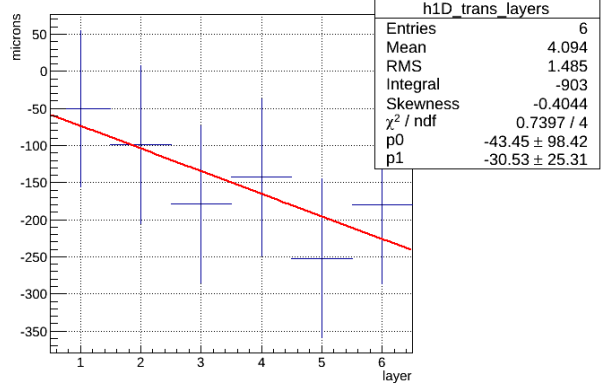

Fig. III.14. Mean x residual (μm) vs layer number for ME+1/3/17 **with** low occupancy "box" removed.
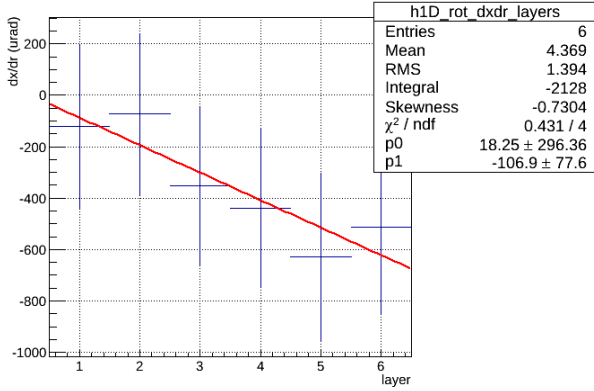

Fig. III.15. Mean rotation ($\frac{d\Delta x}{dr}$) (μrad) vs layer number for ME+1/3/17 **without** low occupancy "box" removed.
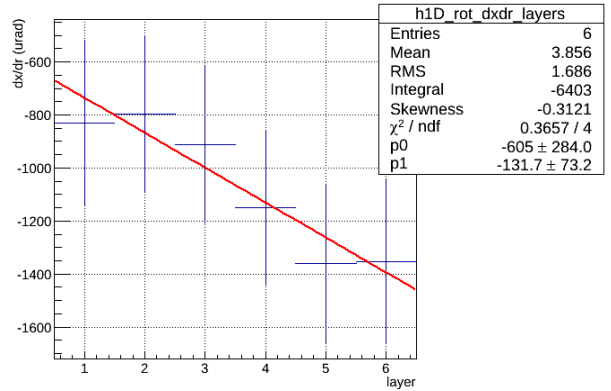

Fig. III.16. Mean rotation ($\frac{d\Delta x}{dr}$) (μrad) vs layer number for ME+1/3/17 **with** low occupancy "box" removed.

Result

After implementing a fiducial selection requirement in the low occupancy "box", average x offsets (Figs. III.13, III.14) for each layer shifted by almost 90 microns, which is under half of the x offset ($\sim 200\ \mu$m) caused by chamber edge effects. Here, however, relative shifts between layers become more pronounced post-selection, suggesting a significant impact of this low occupancy region on relative layer effects. The "box" selection requirement created

27

a 0.6 milliradian rotation for the chamber (Figs. III.15, III.16) which is also comparable with a ϕ_z rotational offset (~ 0.9 mrad) caused by chamber edge effects. This proves that applying fiducial selection requirements to low occupancy areas is essential to improve the precision of the muon alignment procedure.

Conclusions

The event prefilter that has been previously used by the alignment procedure caused DT segments in the barrel to undesirably affect the alignment procedure of the endcap CSCs. This is directly remedied by modifying the prefilter so that muon tracks are required to cross one or more muon chambers (previously, 2 or more chambers were required).

In the general case of any CSC, fiducial selection requirements on the edges of chambers should be sufficient to remove unequal pulling effects that might result in bias, causing tracks to preferentially pass one side over the other. Edge selection requirements applied to a chamber demonstrated that removing fiducial tracks had an effect that is comparable to the target uncertainty of the alignment procedure on the endcap chambers for both x offsets and ϕ_z rotation.

For chambers with periodic low occupancy regions (e.g., chamber 17), an innocuous "box" fiducial selection requirement produced a ϕ_z rotation, as well as small relative offsets. Thus, such regions must be carefully treated with additinoal fiducial requirements or compensated by removing a symmetrical "box" on the opposite side of the chamber so they do not introduce any unnecessary biases.

Other chambers with various occupancy-related effects can also be studied in the future to glean information about how the alignment procedure might be affected. In particular, chambers 1 (an example of a "good" chamber), 3 (low occupancy area in center), 11 (malfunctioning strips in center of chamber), and 21 (bottom portion of chamber only has five functioning layers, excluding it from the alignment procedure) all have unique shortcomings which would make them representative candidates for a further comprehensive study

of the ME+1/3 ring. With the developed framework described in this paper, deep analysis of extra chambers is made more straightforward. The resulting improvement in precision of the muon alignment procedure will lead to better muon momentum resolution, which is especially important for searches of new processes beyond Standard Model with TeV muons.

REFERENCES

[1] Lyndon Evans and Philip Bryant. LHC Machine. *JINST*, 3(08):S08001, 2008.

[2] S Chatrchyan et al. The CMS experiment at the CERN LHC. *JINST*, 3, 2008.

[3] The CMS collaboration. The performance of the CMS muon detector in proton-proton collisions at sqrt(s) = 7 TeV at the LHC. *JINST*, 8:1002P, November 2013.

[4] Lucas Taylor. CMS detector design. http://cms.web.cern.ch/news/cms-detector-design.

[5] S Chatrchyan et al. Alignment of the CMS Muon System with Cosmic-Ray and Beam-Halo Muons. *JINST*, 5:T03020, 2010.

[6] The CMS collaboration. Performance of CMS muon reconstruction in pp collision events at $\sqrt{s} = 7$ TeV. *JINST*, 7(10):P10002, 2012.

[7] CMS Collaboration. Aligning the CMS muon chambers with the muon alignment system during an extended cosmic ray run. *JINST*, 5(03):T03019, 2010.

[8] F. James and M. Roos. Minuit - a system for function minimization and analysis of the parameter errors and correlations. *Computer Physics Communications*, 10(6):343 – 367, 1975.

[9] R. Brun and F. Rademakers. ROOT. http://root.cern.ch, 2004.